The presence of a ground fog is not unexpected, and has been discussed in recent papers by Flasar and Goody (*7*), Hess (*8*), and Farmer (*3*). While this is a possible explanation for the observed diurnal behavior (at 10°,83°), we cannot at present entirely rule out the release of vapor from ice entrained in the topmost layer of the regolith material, or the gradual reduction of opacity of a higher-elevation cloud layer above the vapor, as possible alternate explanations. Unfortunately, we have not yet obtained any high-altitude images of this area to aid in the interpretation of the data.

A further inference can be drawn from the fact that, since the vapor is still increasing at the time of the last diurnal observation, ~1300 hours, it is reasonable to assume that there is still some condensate in the atmosphere or near-surface layer at that time. This result suggests that some fraction of the water remains in the solid phase throughout the day; one interpretation of the latitude–time of day trend shown in Fig. 2 is that this fraction increases toward the northern midlatitudes. Hence we might expect that, as the northern summer progresses, the lower latitude limit of the atmospheric condensate layers will recede, with a corresponding increase in the fractional amount of ice vaporized during the day, and a decrease in the amplitude of the diurnal vapor cycle as the vapor becomes mixed into the bulk atmosphere above the boundary layer trap. At this stage the meridional circulation will carry the vapor to the cooler latitudes (principally the winter hemisphere).

The Viking 1 orbital observations conveniently cover the period of the northern water vapor growth and decay, and the second spacecraft (Viking 2 orbiter) will give good polar coverage of the latter stages of this phase. The extended mission, with both spacecraft, will enable the progression of the seasonal cycle into the southern hemisphere to be followed. The mission plans for the orbiters thus present an excellent opportunity during the forthcoming months to study the variability of the vapor and its interaction with the surface of the planet over a wide range of spatial and temporal scales, and to test the validity of some of the theories which have been proposed to explain its cyclic behavior.

CROFTON B. FARMER
DONALD W. DAVIES
Jet Propulsion Laboratory, California Institute of Technology, Pasadena 91103
DANIEL D. LAPORTE
Santa Barbara Research Center, Goleta, California 93017

References and Notes

1. For a discussion of the orbit geometry and the corresponding opportunities for observational coverage, see G. A. Soffen and C. W. Snyder, *Science* **193**, 759 (1976).
2. See E. S. Barker, *Icarus* **28**, 247 (1976), and references contained therein.
3. C. B. Farmer, *ibid.*, p. 279.
4. ——— and D. D. LaPorte, *ibid.* **16**, 34 (1972).
5. R. A. Schorn *et al., ibid.* **11**, 283 (1969); R. G. Tull, *ibid.* **13**, 43 (1970).
6. Day and night vertical profiles of temperature for this region of the planet at this season were obtained from Mariner 9 (IRIS); see B. Conrath *et al., J. Geophys. Res.* **78**, 4267 (1973). The expected small variation in the diurnal temperature extremes for the bulk atmosphere above the boundary layer was first discussed by P. Gierasch and R. Goody, *Planet. Space Sci.* **16**, 615 (1968).
7. F. M. Flasar and R. M. Goody, *Planet. Space Sci.* **24**, 161 (1976).
8. S. L. Hess, *Icarus* **28**, 269 (1976).
9. A large number of people have contributed to the design and construction of the flight instruments, which have operated flawlessly, and to the development of the special-purpose computer and its software system used for the data analysis. We are grateful to all of these, whose enthusiastic involvement has ensured the success of the experiment. We thank especially W. Carls, H. Clark, J. Geiselman, E. Goldyn, S. Hanson, A. Holland, R. Kares, R. Killian, D. Langford, F. Murphy, J. Riccio, and D. Rupnik for their considerable efforts over the past months: this is submitted on their behalf. This report presents the results of one phase of research carried out at the Jet Propulsion Laboratory under NASA contract NAS 7-100.

26 July 1976

Infrared Thermal Mapping of the Martian Surface and Atmosphere: First Results

Abstract. *The Viking infrared thermal mapper measures the thermal emission of the martian surface and atmosphere and the total reflected sunlight. With the high resolution and dense coverage being achieved, planetwide thermal structure is apparent at large and small scales. The thermal behavior of the best-observed areas, the landing sites, cannot be explained by simple homogeneous models. The data contain clear indications for the relevance of additional factors such as detailed surface texture and the occurrence of clouds. Areas in the polar night have temperatures distinctly lower than the CO_2 condensation point at the surface pressure. This observation implies that the annual atmospheric condensation is less than previously assumed and that either thick CO_2 clouds exist at the 20-kilometer level or that the polar atmosphere is locally enriched by noncondensable gases.*

Experiment description. The Viking infrared thermal mapper (IRTM) contains four telescopes, each with seven detectors. Thermal emission from the planet's surface is measured in four bands, 6.1 to 8.3, 8.3 to 9.8, 9.8 to 12.5, and 17.7 to 24 μm; there are three detectors in each of the first two bands and seven in each of the last two. One detector at 14.56 to 15.41 μm, centered on the CO_2 vibration band, measures the stratospheric temperature. Brightness temperatures in these bands are identified as T_7, T_9, T_{11}, T_{20}, and T_{15}. Seven detectors at 0.3 to 3.0 μm respond to reflected sunlight.

An objective of this investigation was to achieve good spatial resolution. The field of view is defined by focal plane stops 5.2 mrad in diameter. The spatial response has been measured in the laboratory and verified in flight to be nearly diffraction-limited. In the longest wavelength band, the signal at the planetary limb drops to 10 and 1 percent of maximum when the limb is at distances of 6 and 17 mrad from the center of the field of view. The radiation level is integrated in all channels simultaneously; this arrangement allows measurements of the brightness temperatures and the reflected radiance at seven locations on the planet each 1.12 seconds.

The response of all channels is nearly linear with flux, and is digitized into 1000 data numbers (DN). The maximum response of the solar band corresponds to 75 percent of a perfect white diffuser at normal incidence at the mean Mars distance from the sun. The thermal bands have maximum temperatures between 300 and 330 K. The one-sample noise is less than 1 DN for all channels except T_{15}, where it is about 2.5 DN. The equivalent temperature uncertainty varies with band and temperature; the 7- and 9-μm bands are well on the short wavelength side of the Planck function at 200 K, and only the 20-μm band has good temperature resolution below 170 K.

The angular resolution, detector configuration, sample rate, and scan-platform slew rate were designed to allow approximately uniformly spaced, nonredundant, continuous coverage so that the IRTM experiment can produce two-dimensional images in the solar and thermal bands (*1*). The in-flight performance of the IRTM has been entirely as expected, including some sensitivity to thermal radiation from the Viking lander prior to separation. The results reported here were obtained on revolutions (revs) 3 through 22, occurring over 22 June to 11 July 1976.

Global surface temperatures. From apoapsis to approximately 2 hours before periapsis the entire disk of Mars can be scanned in a single observation sequence. In observations taken near apoapsis, when the disk is largely dark, the major features are the latitude variation expected for the insolation distribution at this season and the rapid rise in temperature after dawn. There is considerable thermal structure in the equatorial region, and a regional low extending northward toward the Chryse Planitia area can be seen.

An example of the view obtained 4½ hours before periapsis as shown in Fig. 1. The disk is half-illuminated, and temperatures rise to above 240 K at noon at the equator. The most conspicuous thermal feature is the minimum of 142 K at dawn, unexpectedly low for the equatorial region, followed by a rapid rise into morning to the east. The minimum is near the summit of the large shield volcano Arsia Mons. The low temperatures near the west limb are in the area of Memnonia Fossae, where clouds or frost were seen after dawn with the approach imaging. Some thermal structure is apparent in the south polar region, where temperatures drop below 140 K.

The thermal behavior of different areas can be more readily seen after the diurnal, latitudinal, and seasonal temperature variations expected for the average martian surface are removed. For this report, we use the temperatures (T_m) from the homogeneous thermal model determined by the Mariner 9 late observations; the model uses bolometric albedo $A = 0.25$ and a thermal inertia $I = 0.0065$ cal cm^{-2} sec$^{-1/2}$ K^{-1} (*2*). The temperature just before dawn is most readily related to the surface physical properties. In the equatorial region, a predawn temperature 10 K above the martian average, if attributed to thermal inertia alone, can be interpreted as about a twofold increase in the average particle size (from 0.3 to 0.6 mm) or as a 25 percent increase in the area of large blocks or exposed bedrock.

The differences ($T_{20} - T_m$) for predawn portions of the data in Fig. 1 and in an apoapsis sequence 8 hours earlier are shown on a Mercator projection in Fig. 2. The two observation sequences show comparable behavior south of $-20°$, and there is little structure between $-40°$ and $-65°$ latitude, with the exception of a cold region over the Argyre basin. The area on the Tharsis ridge west of Arsia Mons is as much as 18 K colder than expected for average martian surface material. The major canyon areas are generally warm, from Coprates Chasma eastward and northward to Chryse Planitia and Acidalia Planitia. These two regional extremes of residual temperature correspond to topographic

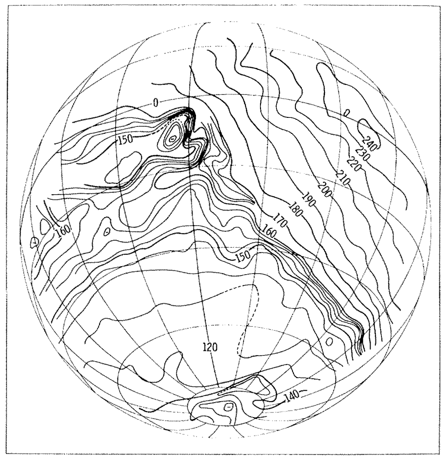

Fig. 1. Perspective view of T_{20} observed 4½ hours before periapsis at an altitude of 22,000 km on rev 10 on 29 June 1976. The contour interval is 2 K over the night area and 10 K over most of the illuminated disk. Latitude and longitude lines are shown every 20°. The nighttime minimum and rapid dawn heating near $-10°$, 120° are in the region of Arsia Mons volcano. Closed contours in all figures are positive unless identified as depressions.

high and low areas, respectively. The variation of thermal conductivity with gas pressure expected for the average martian surface material can account for about one-third of the residual temperature for these two large areas.

There is considerable thermal structure at the resolution limits of these observations in the canyon areas, suggesting geologic heterogeneity. The morphology in the canyon areas indicates that a variety of processes have been active (*3*). There is some correlation of other warm regions with the areas depicted as dark features in the Mariner 9 maps.

Solar reflectance. Measurements of the surface brightness in absolute units are being obtained in the solar band. A contour map, with about 130 km resolution, of brightness normalized to the solar irradiance is shown in Fig. 3. These data were obtained simultaneously with the thermal data shown in Fig. 1. The phase of Mars was very nearly 90° during the observations, so the terminator bisects the disk, and, if the planet were of uniform Lambert albedo (A_L) (*4*), all brightness contours would parallel the terminator. Were the surface locally flat and Lambertian, the contour intervals would be uniformly spaced from terminator to bright limb.

In Fig. 3 several features can be noted:

1) There is a tendency for A_L to increase toward the limb, particularly near the northern terminator. This effect is possibly a consequence of scattering by haze in the martian atmosphere.

2) The mean A_L is near 0.25, and its variations are correlated with many classical light and dark areas identified from Earth-based observations in the much narrower visual wavelength band. For example, Juventae Chasma ($-6°$, 62°) and Eos Chasma ($-17°$, 55°) regions appear darker than their surroundings, whereas Syria Planum ($-12°$, 83°) and eastern Sinai Planum ($-18°$, 67°) regions appear brighter than their surroundings.

3) The visible surface area north of $-10°$ and west of 90° is about twice as reflective as the area south of $-20°$ and west of 50° ($A_L \approx 0.35$ and 0.17, respectively). This northern hemisphere brightness may be due to early morning ground fog or surface ices. This explanation would be consistent with the larger amounts of water vapor detected for this area of the planet during approach observations (*5*). The relative uniformity suggests that the higher reflectivity may be due in part to an intrinsically higher regional surface albedo. The four major volcanoes are included in this area.

4) Argyre Planitia ($-50°$, 40°) is anomalously bright ($A_L \geq 0.35$) as compared to the area immediately to its northwest ($A_L \leq 0.20$). The brightness of Argyre and the surface areas south of Argyre is consistent with the temperature measurements, which show that a major portion of the Argyre basin is at the sublimation temperature of CO_2 ice.

5) The brightness gradients are steeper near the four major volcanoes, particularly near Ascraeus Mons (11°, 106°), most likely as a result of slope effects.

6) The brightness increases rapidly north of the central portion of Coprates Chasma. This may be a result of the unusual geology of this region. Low-altitude observations show the major canyons to have low A_L values. Visual imaging on the plateau north of Coprates suggests an extensive aeolian covering of the underlying geology; this wind-transported material may be brighter than the average material in its source region.

Atmospheric temperatures. The 15-μm channel measures the thermal emission of atmospheric CO_2, weighted by a function with maximum amplitude at 0.63 mbar and half-maximum points at 0.17 and 1.56 mbar for normal viewing (*6*). A typical contour map of T_{15} over the period from dawn to noon is shown in Fig. 4, which does not refer to an isobaric surface on account of varying air mass.

In Fig. 4 and other global maps obtained in the predawn period, the general behavior of stratospheric temperature is characterized by a strong latitudinal dependence in the winter hemisphere and weak diurnal variation. The latter behavior is expected from the prediction of

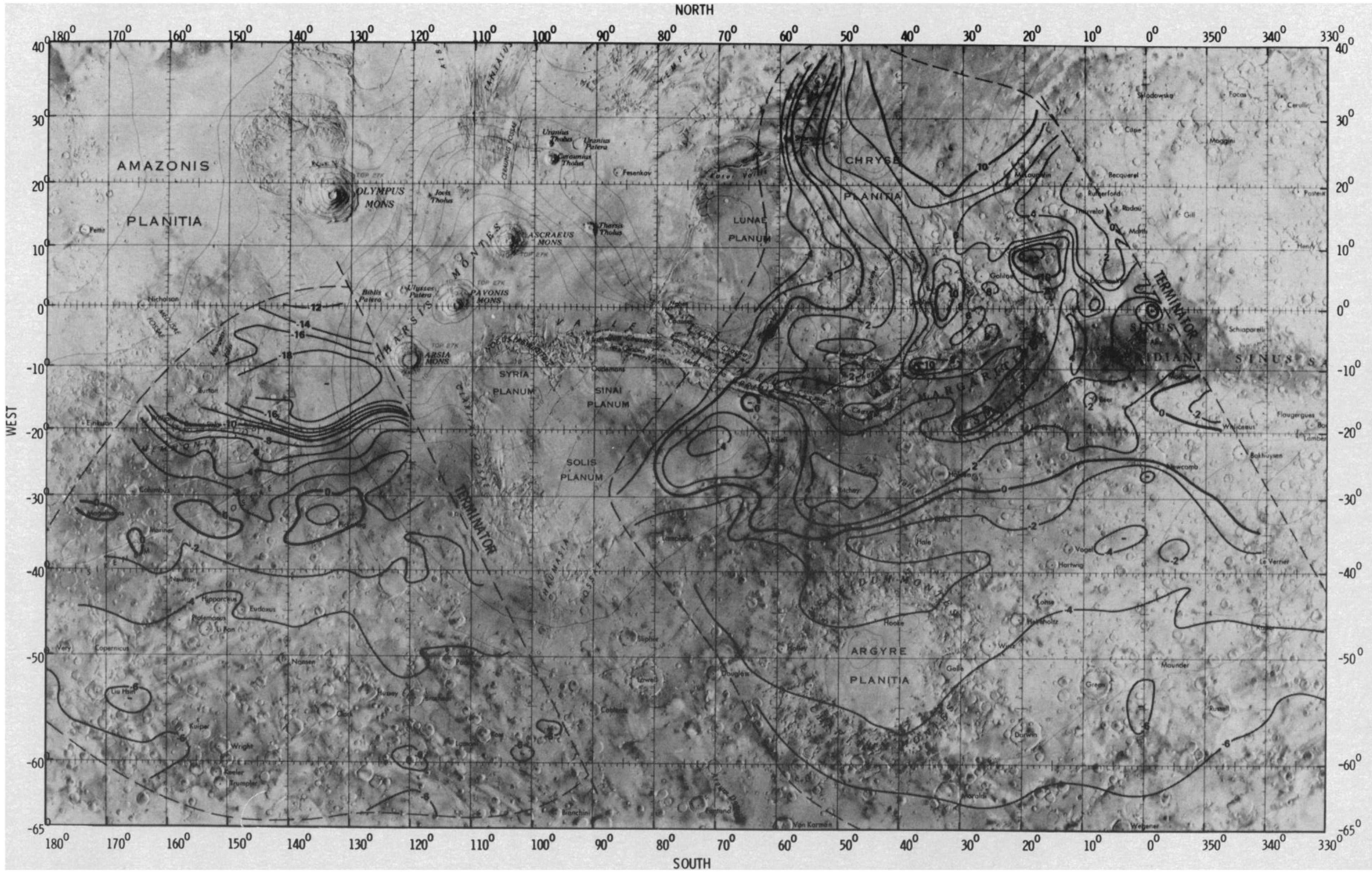

Fig. 2. Mercator map of the residual $T_{20}-T_{m}$ from observations 14 and 4½ hours before the rev 10 periapsis on 29 June 1976. The contour interval is 1 K. The data at the left correspond to the observations shown in Fig. 1. Most of the thermal behavior shown here is attributed to variations in thermal inertia.

general atmospheric temperature models (7). The temperatures measured by the Mariner 9 infrared interferometer spectrometer (IRIS) experiment for the 0.65-mbar level at the same season (areocentric longitude of the sun $L_s = 97°$) and latitude $+20°$ are very similar to the T_{15} values near dawn shown in Fig. 5, which displays surface and atmospheric temperatures specific to the region of the Chryse landing site. In the afternoon, however, T_{15} is about 10 K higher than the IRIS temperatures. The origin of this discrepancy has not been clarified, but it could arise from the grossly different field of view of the two experiments or as a result of a manifestation of temporal changes in the martian atmosphere.

The southernmost latitudes, only partly shown in Fig. 4, reveal surprisingly low stratospheric temperatures, well below those found in the IRIS experiment for polar regions (8). The temperature uncertainty of a single measurement for T_{15} (140 K) is $\simeq$ 5 K, but averaged data show clearly that temperatures below 136 K, near the CO_2 condensation point at stratospheric pressures, do occur south of $-70°$ latitude. The T_{15} measurements do not represent a constraint on the formation of CO_2 clouds in these latitudes.

Local areas. Orbiter observations thus far have emphasized potential landing areas, this being especially true for high-resolution observations. The determination of diurnal thermal behavior from the Viking 1 synchronous orbit is compromised by the low resolution accessible for predawn observations; the predawn spatial resolution decreases rapidly north of the equator, and no predawn observations are possible north of 35°. Three areas considered as Viking landing sites are discussed below.

Chryse. The measurements of T_{11} for the Chryse Planitia are shown in Fig. 5. The morning data have been collected within the $+20°$ to $+24°$ latitude and 46° to 49° longitude area over several revolutions. Variations in thermal inertia within this area can account for the scatter in the morning data. At 0600 hours, areas with thermal inertia differing by 0.001 in the vicinity of $I = 0.008$ would show a temperature difference of 2 K. The data near 1500 to 1600 hours in Fig. 5 refer to the smaller area between $+22.0°$ and $+23.2°$ latitude and 47° to 48° longitude (9). The homogeneous thermal model which best fits the morning T_{11}, based on the use of A equal to the value $A_L = 0.26$ measured in the solar band, is obtained with $I = 0.009$ (10). However, there is clear disagreement between this model and T_{11} measured in the afternoon. These departures of T_{11} from the predictions can be explained by several effects not considered in the simple model:

1) An admixture of materials with low and high thermal inertia is suggested by the existence of rocks at the Viking 1 landing site (11). Two-component flat models which account for the predawn temperatures fail, however, to predict afternoon temperatures as low as those observed. The observation geometry at the landing sites has been optimized for visual imagery, the resolution of which improves toward angles of solar incidence near 70°. In addition, the westward search for the eventual Viking 1 landing site resulted in oblique viewing such that the IRTM afternoon observations preferentially include the shaded faces of rocks and their shadows. The A_L values derived from observations at a time of day when shadows are present will underestimate A. Inclusion of these effects into simplified models leads to predicted temperatures more nearly in agreement with the observations. Local variations in these effects within the afternoon areas could explain the scatter found in the measurements.

2) The existence of a regional atmospheric haze, revealed by orbital imagery over the landing areas, may also help to explain the discrepancy between the measured afternoon surface temperatures and those predicted by the thermal models which disregard the presence of clouds. If clouds are sufficiently opaque; they impede solar heating of the surface, thereby reducing temperature.

3) Increased thermal coupling between the ground and atmosphere in the afternoon would tend to decrease surface temperatures. This last effect was suggested to explain the departures of the Mariner 9 observations from the homogeneous model predictions in the region of $+10°$ to $+40°$ latitude (2). However, implausibly high winds are required if the discrepancy is to be explained by this effect alone.

Capri. This region is bounded on the

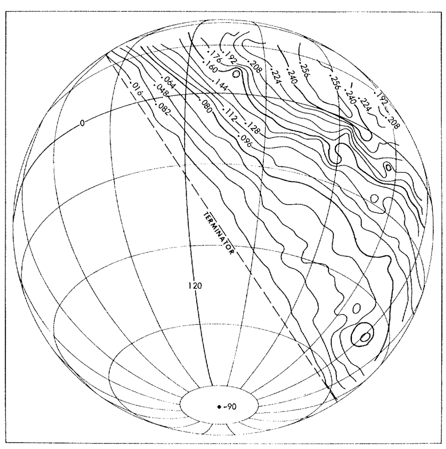

Fig. 3. Perspective view of solar band brightness obtained at the same time as the data in Fig. 1. The units are brightness relative to that of a white Lambert surface with normal incident sunlight. Brightness contours for such an ideal surface would parallel the terminator and be uniformly spaced. Latitude and longitude lines are shown every 20°.

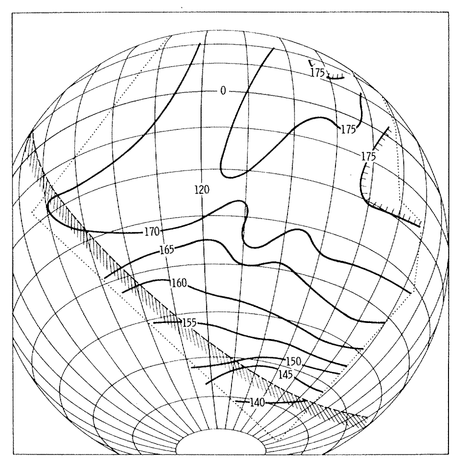

Fig. 4. Dawn-to-midday behavior of stratospheric atmospheric temperatures. Observations were made on rev 9 at a range of 12,000 km. The nominal sampled pressure level is 0.63 mbar at air mass 1.0. No correction has been made to account for the sampling of greater altitudes toward the limb. Latitude and longitude lines are shown every 20°.

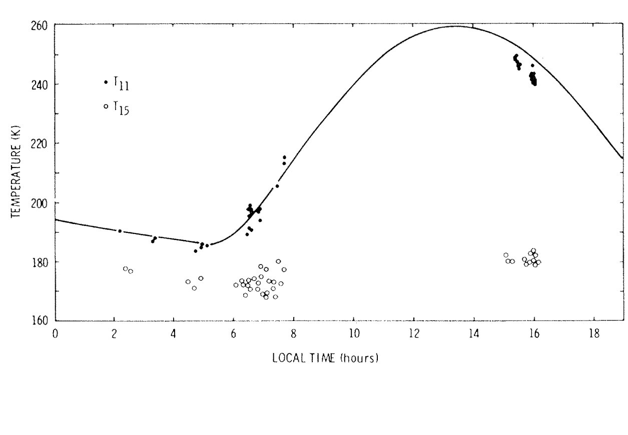

Fig. 5. Diurnal surface and atmospheric temperature variation in the Chryse region. Closed circles represent T_{11} measurements within the area bounded by latitudes $+22°$, $+23.2°$, and longitudes 47°, 48°. The curve depicts the surface temperature prediction for $A = 0.26$, $I = 0.009$. Open circles represent atmospheric temperatures within the area bounded by latitudes $+21°$, $+24°$, and longitudes 40°, 56°; measurements are reduced to the 0.63 mbar level (air mass, 1.0).

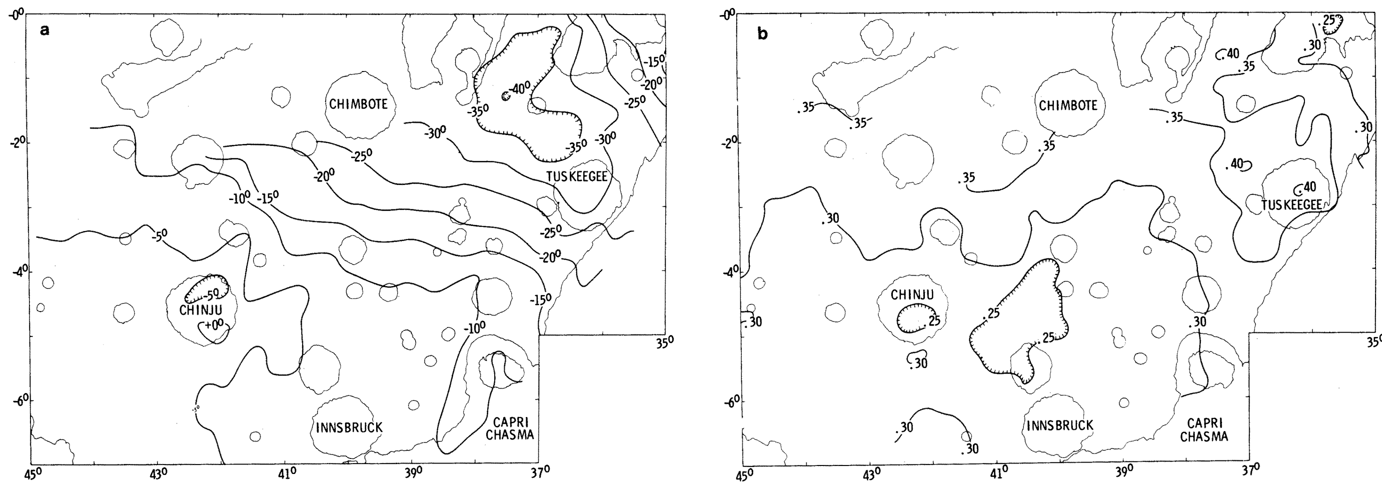

Fig. 6. (a) Thermal relief map of the Capri region at 1530 hours. The contours shown are 5 K apart and represent the difference between T_{11} and T_m. The model uses an A value of 0.25 and an I value of 0.0065 cal cm^{-2} sec$^{-1/2}$ K^{-1}. The dark irregular line near the bottom is the north rim of the Gangis and Capri Chasma. The substantial thermal depression, with deviations in $T_{11} - T_m$ to -40 K, must be due to clouds. (b) Map of A_L values of the Capri region. The contours shown on this map [which is the same scale and projection as (a)] were derived from radiances measured in the 0.3- to 3-μm band. A comparison with (a) indicates general agreement in the sense that temperatures are lower where the albedo is higher, but the highest albedo, 0.40, is by itself insufficient to explain the magnitude of the thermal depression.

south by the Gangis and Capri Chasma and extends in the north to the equator. A sketch of some of the prominent features in this region is shown in Fig. 6a. This region was mapped once at low altitude on rev 11. The local Mars time at the center of the region was 1530 hours, the viewing angle varied between 35° and 70°, and the observation range varied between 2000 and 2500 km.

This region exhibits the largest thermal relief seen in any of the high-resolution mapping data yet collected, as shown in Fig. 6a. The thermal structure in this region is dominated by the large depression in the northeast, where the temperature deviates 40 K from the thermal model. A comparison of the thermal differences (Fig. 6a) with the A_L values observed at the same time (Fig. 6b) indicates general agreement, in the sense that the temperature depression corresponds to a region of high A_L. But this A_L increase by itself is insufficient to explain the temperature depression since the expected change in temperature with A at this time of day is $\simeq -8$ K per 0.1 change in A. Clouds are common in images of this region taken on rev 14 at this time of day but they appear not to be substantial enough to account for the observed thermal results. Although the four thermal channels exhibit parallel behavior over this feature, the depth of the thermal depression in T_7 is only half that observed for the other bands. Mariner 9 spectra indicate that the 9-μm band should be the least affected by H_2O ice clouds (*12*). Although an H_2O cloud is the least unlikely cause of this feature, the relative spectral behavior remains to be explained.

Cydonia. In contradistinction to Capri, the Cydonia region (4° to 13° longitude, 42° to 46° latitude) appears as predicted thermally. The $T_{11} - T_m$ contrast across the region is less than 10 K, and the thermal relief agrees with geologic boundaries mapped in photographs taken on rev 9. The ejecta blankets of the two largest craters in the region [DK and DKb in MC-4 (*13*)] stand above the mantled terrain to the east and the polygonally patterned terrain to the west. Although variations in thermal inertia cannot be inferred directly from observations at this time of day (1800 hours), it seems apparent that a mappable thermal behavior is being caused by variation of some surface physical property, such as surface texture, associated with the identified geologic units.

South polar region. The Viking 1 orbit allows viewing of the southern hemisphere, to the south pole, when the spacecraft is about 3 hours before periapsis. Observation scans of the planet covering the south polar region have yielded brightness temperatures well below those reported by the infrared radiometers and spectrometers on Mariner 7 and Mariner 9 (*14*). Earlier measurements of the brightness temperatures of the southern and northern polar caps made during the spring and summer seasons were near 148 K, as expected for solid CO_2 subliming at a pressure of about 6 mbar. There are no earlier observations of any kind of the midwinter polar regions.

The T_{20} values measured by the IRTM over the south polar region on rev 22 are shown in Fig. 7. Observations were made during two scan patterns, each of which went off the dark limb of the planet, allowing the zero flux point to be accurately determined. There is a strong temperature gradient southward to $-50°$, where T_{20} reaches approximately 148 K. The temperatures decrease less rapidly to 145 K, and there follows a broad thermal plateau between 145 and 143 K, which constitutes most of the polar region. Poleward from $-70°$, T_{20} shows considerable structure. In addition to a sharp minimum of approximately 134 K, there are several arcuate lows which extend outward from the geographic pole. These cool regions have a temperature contrast of 2 to 3 K and a breadth of approximately 200 km, with a form resembling that of terrestrial polar troughs.

Where T_{20} is greater than 150 K, north of $-50°$, the stratospheric temperature, T_{15}, shows small variation from 167 K. Across the plateau in T_{20} at 143 to 145 K, T_{15} decreases steadily poleward, from 165 K to less than 145 K. South of this plateau, where T_{20} is less than 141 K, T_{15} varies from 145 K down to about 130 K. At 140 K, the noise equivalent temperatures in T_{15} and T_{20} are approximately 4.5 and 0.5 K, respectively. Although simultaneous measurements are made in these two channels, since the T_{20} thermal contrast near the geographic pole is only marginally greater than the noise in T_{15}, it is unlikely that a correlation can be obtained without further observations that would allow averaging of the 15-μm temperatures.

Although not shown in Fig. 7, T_{15} exhibits sharp limb brightening, rising up to 150 K in the last sample on the planet. This temperature is approximately that expected for the atmosphere on the geometric limb, based on T_{15} measurements at the corresponding latitudes nearer the subspacecraft point.

Simultaneous measurements of T_{11} and T_{20} show a strong correlation over the polar region. Where T_{20} is less than 150 K, the mean variance in $T_{11} - T_{20}$ is less than the T_{11} digitization limit (2 K at 140 K). This finding suggests that the two wavelengths are sampling the same region, whether on the surface or in the atmosphere.

There are several mechanisms which individually or collectively could be invoked to explain such low values of T_{20}. These are low emissivity, the presence of clouds, high surface elevations, cyclonic low pressures, or dilution of CO_2 by noncondensable gases. Although more than one of these effects is likely to be contributing, it is simplest to evaluate them independently, under the assumption of a mean surface pressure of 6.1 mbar of CO_2 at mean Mars elevation, with a corresponding saturation temperature of 147.7 K.

If the surface kinetic temperature were 148 K, the minimum brightness temperature observed, 132 K, would require an emissivity of 0.58. Although the emissivity of a pure CO_2 frost is not known, this value seems implausibly low for a natural rough surface. The broad thermal plateau beginning at 145 K suggests that this region is completely covered with CO_2 and has a uniform kinetic temperature near 148 K. This temperature corresponds to a frost emissivity of 0.92. Such an emissivity partly accounts for the lower temperatures measured near the geographic pole.

The other four explanations are all equivalent to lowering the partial pressure of CO_2 over the region sensed at 20 μm; the minimum required partial pressure is 0.46 mbar. This could be accomplished if clouds were present at an elevation of 19 km above the mean martian surface. Imagery obtained simultaneously with these observations shows a remarkably clear atmosphere north of the polar night. The clear atmosphere at $-50°$ seen in limb imaging is in concert with thermal results, which show the temperature at 0.63 mbar to be about 163 K, well above the CO_2 condensation temperature. Poleward of $-65°$, T_{15} is below T_{20}, and extensive CO_2 clouds are possible (visual imaging is not).

Surface elevations of 19 km could also be invoked to explain the observed temperatures. However, elevation determinations in the south polar region by radio occultation, IRIS, and ultraviolet spectrometry, while generally of lower quality than for more temperate regions, do not indicate unusually high values (greater than 5 km). Also, imaging observations do not indicate large topographic variations.

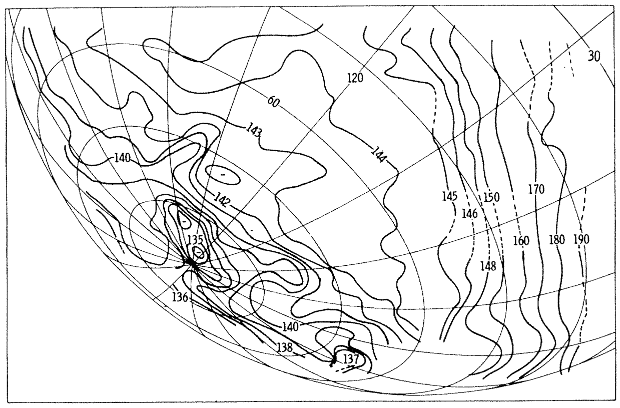

Fig. 7. Brightness temperatures at 20 μm in the south polar region. The contour intervals are 1 K below 145 K and 10 K above 150 K. Longitude lines are spaced by 20° and latitude lines by 10°. The minimum temperature of 134 K is well below that expected for surface CO_2 condensation. The arcuate low-temperature regions extending from the pole are similar to terrestrial winter circulation patterns. It is not certain whether the observed temperatures represent the surface or high clouds.

The CO_2 partial pressure will be lowered through dilution by an accumulation of noncondensable minor constituents. As the net radiation loss causes CO_2 condensation and the atmosphere moves to maintain constant total pressure, the concentration of noncondensable gases increases locally. The magnitude of CO_2 dilution—noncondensable gas enrichment—depends on the relative time scales of CO_2 condensation and mixing of CO_2 depleted "old" polar atmosphere with "fresh" atmosphere from the nonpolar regions. The time scale required for the atmosphere to be enriched by a noncondensable gas is 44 days, the period over which a blackbody at 144 K radiates the latent heat of condensation of the CO_2 contained in an atmospheric column.

If condensation is occurring at the surface, near-surface enrichment of a noncondensable gas could occur with a very short time scale. For example, the lowest 100 m could acquire a 16-fold enrichment in about 10 days. The first results from the Viking entry mass spectrometer (*15*) indicate that about 5 percent of the martian atmosphere is composed of argon, nitrogen, and oxygen, which would not condense under martian polar conditions. A 16-fold increase to 80 percent would lower the CO_2 condensation temperature to 137 K. The resulting low-temperature, near-surface layer might be stable, notwithstanding an adverse stratification of the molecular weight.

Finally, dynamic meteorological processes are unlikely to lower the atmospheric pressure at an equipotential surface by more than 1 mbar (*16*).

On the basis of the available data, it is not possible to discriminate between the high-cloud and the low-level dilution hypothesis. Further observations of possible time changes or motion of the polar thermal structure may allow such a distinction to be made.

Whichever explanation is correct, the net flux emitted by the polar region south of $-55°$ is 85 percent of that emitted by a uniform 147.7 K surface over this region. To the extent that this behavior holds throughout the polar winter, the amount of atmospheric condensation and the concomitant annual variation in surface pressure, considering the southern hemisphere only, are correspondingly less than in existing theories.

HUGH H. KIEFFER
University of California, Los Angeles 90024
STILLMAN C. CHASE, JR.
Santa Barbara Research Center, Goleta, California 93017
ELLIS D. MINER
FRANK DON PALLUCONI
Jet Propulsion Laboratory, California Institute of Technology, Pasadena 91103
GUIDO MÜNCH, GERRY NEUGEBAUER
California Institute of Technology
TERRY Z. MARTIN
University of California, Los Angeles

References and Notes

1. A description of the IRTM instrument and investigation at the conceptual design stage has been given by H. H. Kieffer *et al.* [*Icarus* **16**, 47 (1972)]. The major differences are the actual use of four small (9-cm aperture) telescopes, a "V" pattern detector configuration, and the inclusion of the 15-μm channel.
2. H. H. Kieffer, S. C. Chase, Jr., E. Miner, G. Münch, G. Neugebauer, *J. Geophys. Res.* **78**, 4291 (1973).
3. H. Masursky, *ibid.*, p. 4009.
4. Lambert albedo is herein defined as the ratio between the measured radiance *R* in the solar band and the incident flux

$$A_L = \frac{\pi U^2 R}{F \cos i}$$

where *F* is the solar constant, *U* is the distance from the sun in astronomical units, and *i* is the incidence angle.
5. C. B. Farmer, D. W. Davies, D. D. LaPorte, *Science* **193**, 776 (1976).
6. The pressure sampled at normal viewing was derived under the assumption that the atmo-

spheric temperature profile has a shape given by the mean Viking engineering model (NASA Langley Research Center M75-125-2).
7. P. Gierasch and R. Goody, *Planet. Space Sci.* **16**, 615 (1968).
8. B. Conrath, R. Curran, R. Hanel, V. Kunde, W. Maguire, J. Pearl, J. Pirraglia, J. Welker, T. Burke, *J. Geophys. Res.* **78**, 4267 (1973).
9. An oversight in currently used ground software produces geometry errors that can have a maximum value of 3/8° in the direction of scan platform motion. That uncertainty has been removed by hand from maps used in this report but remains in the morning data of Fig. 5, contributing to the scatter there to an unknown degree.
10. Predawn air temperatures measured 167 cm above the surface during the first day after landing as part of the lander meteorology experiment show excellent agreement with the predawn T_{11} values.
11. T. A. Mutch, A. B. Binder, F. O. Huck, E. C. Levinthal, S. Liebes, E. C. Morris, W. R. Patterson, J. B. Pollack, C. Sagan, G. R. Taylor, *Science* **193**, 791 (1976).
R. J. Curran, B. J. Conrath, R. A. Hanel, V. G. Kunde, J. C. Pearl, *ibid.* **182**, 381 (1973).
13. The MC charts are a set of 30 topographic shaded relief maps (scale, 1 : 5 × 10^6) produced by the Department of the Interior, U. S. Geological Survey, Reston, Va. 22092.
14. K. C. Herr and G. C. Pimentel, *Science* **166**, 496 (1969); G. Neugebauer, G. Munch, H. H. Kieffer, S. C. Chase, Jr., E. Miner, *Astron. J.* **76**, 719 (1971); R. Hanel, B. Conrath, W. Hovis, V. Kunde, P. Lowman, W. Maguire, J. Pearl, J. Pirraglia, C. Prabhakara, B. Schlachman, G. Levin, P. Straat, T. Burke, *Icarus* **17**, 423 (1972).
15. A. O. Nier, W. B. Hanson, A. Sieff, M. B. McElroy, N. W. Spencer, R. J. Duckett, T. C. D. Night, W. S. Cook, *Science* **193**, 786 (1976).
16. S. Hess and C. Leovy, personal communication.
17. The two Viking IRTM experiments represent a fourfold increase in the total number of thermal detectors flown to other planets. Their success is the result of the individual efforts of a large number of people during design, fabrication, and the complex flight operations of this instrument. The prolonged efforts of Mike Agabra, Jack Engel, Howard Eyerly, Claude Michaux, Richard Ruiz, and Don Schofield are representative of this group. The massive data reduction system is a tribute to and from Bob Mehlman, John Gieselman, and Elliot Goldyn. We hope all involved take satisfaction from this evidence of their effort. Supported by Jet Propulsion Laboratory contract 952988 to the University of California.

26 July 1976

Composition and Structure of the Martian Atmosphere: Preliminary Results from Viking 1

Abstract. *Results from the aeroshell-mounted neutral mass spectrometer on Viking 1 indicate that the upper atmosphere of Mars is composed mainly of CO_2 with trace quantities of N_2, Ar, O, O_2, and CO. The mixing ratios by volume relative to CO_2 for N_2, Ar, and O_2 are about 0.06, 0.015, and 0.003, respectively, at an altitude near 135 kilometers. Molecular oxygen (O_2^+) is a major component of the ionosphere according to results from the retarding potential analyzer. The atmosphere between 140 and 200 kilometers has an average temperature of about 180° ± 20°K. Atmospheric pressure at the landing site for Viking 1 was 7.3 millibars at an air temperature of 241°K. The descent data are consistent with the view that CO_2 should be the major constituent of the lower martian atmosphere.*

The Viking spacecraft which landed on Mars on 20 July 1976, about 4 hours after local noon, included a set of instruments which measured the physical and chemical properties of the martian atmosphere during entry. The upper atmosphere, above about 100 km, was sampled with a mass spectrometer sensitive to neutral gases in the mass range 1 to 50. Properties of the martian ionosphere were determined with a planar retarding potential analyzer (RPA) designed to provide information on the temperature, composition, and concentration of atmospheric ions. The RPA, which also measured electron energy spectra, was expected in addition to clarify the nature of the interaction between Mars and the external solar wind. The RPA and the upper atmospheric mass spectrometer (UAMS) were mounted on the spacecraft aeroshell. Pressure, temperature, and acceleration sensors gave data on the structure of the atmosphere below 100 km. These results, combined with information from the spacecraft's gyroscopes and radar altimeter, allow one to determine the variation of atmospheric density, pressure, temperature, and winds over an extensive height range for the lower atmosphere.

In this report we present a preliminary account of the results obtained from the various entry science experiments. More detailed accounts of the instruments are given elsewhere (*1*). The UAMS employed an open ion source mounted in such a manner as to allow ambient atmosphere to enter the instrument directly, an important design feature which permits a qualitative measurement for reactive gases such as O. The concentration of chemically inert species may be determined with some confidence from laboratory calibrations obtained prior to flight. The instrument was also exposed to a high-speed molecular beam designed to simulate motion of the spacecraft through the martian atmosphere. These data allow one to establish a quantitative relation between measured quantities and ambient atmospheric densities (*2*).

A spare instrument, identical to the flight instrument, was set up in the laboratory to facilitate a number of studies not possible in preflight tests. Figure 1 reproduces a variety of spectra obtained with pure CO_2, CO_2 with 2 percent Ar, and CO_2 with 5 percent N_2. The mass peaks at 44, 28, 22, 16, and 12 in Fig. 1a correspond to CO_2^+, CO^+, CO_2^{2+}, O^+, and C^+, respectively. The incident electrons in Fig. 1, and for the martian spectra shown in the other figures, have energies equal to 75 ev. Figure 1a also indicates mass peaks at 46, 45, 30, 29, 23, 22.5, and 13, due to $(^{12}C^{16}O^{18}O)^+$, $(^{13}C^{16}O^{16}O)^+$, $(^{12}C^{18}O)^+$, $(^{13}C^{16}O)^+$, $(^{12}C^{16}O^{18}O)^{2+}$, $(^{13}C^{16}O^{16}O)^{2+}$, and $(^{13}C)^+$. Mass peaks at 32 and 14 are associated with a small quantity of O_2^+ and CO^{2+} formed during the ionization of CO_2. Peaks at 17 and 18 are due to residual concentrations of H_2O present as an impurity in the instrument. Addition of Ar (Fig. 1b) gives rise to peaks at 40 and 20. The peak at 28 is approximately doubled by addition of 5 percent N_2 (Fig. 1c), and the presence of N_2 is further confirmed by the peak at mass 14 due to N^+ and $(N_2)^{2+}$.

Figure 2 gives a sample spectrum for Mars obtained at an altitude of approximately 135 km above the martian surface. Prominent peaks at masses 40 and 20 show clear evidence for Ar. The mixing ratio for the gas at this altitude, relative to CO_2, is approximately 0.015 by volume, in major disagreement with an indirect measurement of Ar inferred from data obtained by the Soviet probe Mars 6. Istomin and Grechnev (*3*) reported a mixing ratio of 0.54 ± 0.2 for an inert constituent of the martian atmosphere which they attributed to Ar. The mixing ratio of ^{40}Ar in the lower martian atmosphere cannot be this high and must lie somewhere in the range 0.01 to 0.02.

The peak at mass 28 in Fig. 2 contains contributions from CO^+ formed by the ionization of CO_2 and CO, in addition to N_2^+ formed by the ionization of N_2. The peak at mass 14 is composed primarily of N^+ and $(N_2)^{2+}$ from N_2, although it includes also a small contribution from $(CO)^{2+}$ formed by the ionization of CO_2 and CO. The data in Fig. 2 indicate a mixing ratio of N_2 relative to CO_2 of about 0.06. Much higher mixing ratios were detected at higher altitude, as would be expected as a result of the diffusive separation of the lighter gas, N_2. A preliminary attempt to extrapolate the present data to lower altitude suggests a mixing ratio, N_2 to CO_2, of between 0.02 and 0.03 for the bulk atmosphere, consistent with an upper limit for this parameter imposed earlier (*4*) based on analysis of the ultraviolet day glow spectra measured by Mariner 6 and Mariner 7 (*5*).

The peak at mass 32 is due primarily to O_2 and suggests a mixing ratio, O_2 to